Mechanism for selective initialization of silicon-vacancy spin qubits with $S = 3/2$ in silicon carbide

Jeongeun Park,[1] Seoyoung Paik,[1] Seung-Jae Hwang,[1] Di Liu,[2] Öney O. Soykal,[3] Joerg Wrachtrup,[2] and Sang-Yun Lee[1,*]

[1] *Department of Physics and Photon science, Gwangju Institute of Science and Technology, Cheomdan-gwagiro 123, Gwangju, Republic of Korea*

[2] *3rd Institute of Physics, IQST, and Research Centre SCoPE, University of Stuttgart, Stuttgart, Germany*

[3] *Photonic Inc., Vancouver, Canada*

(Received 16 July 2023; revised 18 January 2024; accepted 5 April 2024; published 2 May 2024)

The silicon vacancy in silicon carbide has emerged as a promising quantum system embedded in an industry-friendly platform due to its long-lived spin qubits that can effectively interface with photonic qubits. However, the unique spin quantum number of 3/2 gives rise to a statistical mixture of the optically initialized ground-state spin sublevels, hindering its successful application as a high-fidelity spin-photon interface. Recent experimental breakthroughs have demonstrated a solution to this challenge by achieving pure-state preparation through simultaneous optical initialization and depletion of selected spin sublevels using electron spin resonance. Nonetheless, the underlying mechanism of this process remains poorly understood, and an efficient method for achieving deterministic initialization has not yet been explored. In this work, we present a comprehensive investigation of the selective initialization process by establishing a complete rate model. We offer a detailed explanation of the underlying mechanism and elucidate the trade-off between initialization fidelities and efficiencies, which are strongly influenced by the experimental parameters employed. Through a thorough exploration of a wide range of experimental parameters, we identify the optimal initialization process that allows for pure-state initialization fidelity exceeding 99%. Our study offers valuable insights into achieving high-fidelity spin-photon interface applications, such as quantum repeaters, based on silicon vacancies in silicon carbide.

DOI: 10.1103/PhysRevApplied.21.054005

I. INTRODUCTION

Point defects in semiconductors have been studied as qubits for quantum information technologies [1–3]. Silicon carbide's (SiC) color centers, specifically the silicon vacancies, offer advantages such as stable charge states [4–7], long spin coherence times [4,7–9], and narrow linewidth of emitted photons [4,7], making them ideal for quantum repeaters [2,3,10]. Leveraging advanced silicon semiconductor process technology further supports the development of chip-based quantum information technologies [5,11–18]. The silicon vacancies in 4H-SiC known as the $V1$ center (h site) and $V2$ center (k site) are classified by their zero-phonon line (ZPL) at 862 and 917 nm, respectively. Their ground-state spins serve as a spin qubit [8], and there are ongoing efforts to control the coupled nuclear spins [4,7,8,19]. Previous research identified excited and ground states with quartet manifolds $S = 3/2$ and metastable states with a doublet manifold $S = 1/2$ in both the $V1$ and $V2$ centers [4,8,20]. While the spin-dependent intersystem crossing (ISC) allows the ground-state initialization by only optical excitation, both $V1$ and $V2$ centers are initialized into a mixed state consisting of the equal mixture of $m_S = \pm 1/2$ or $m_S = \pm 3/2$, where m_S are the spin magnetic quantum number. Since ensuring pure-state qubits is crucial for reliable quantum information technology [21], this issue has been extensively studied many times by semiclassical rate models based on the spin-dependent ISC [22–24] and have been experimentally confirmed as well [8,23].

As soon as the radiative and nonradiative transition dynamics had been revealed for both $V1$ and $V2$ centers under the resonant optical transitions to the ZPL [4,23,24], Nagy *et al.* for the $V1$ center [4] and Babin *et al.* for the $V2$ center [7] successfully demonstrated a protocol for the pure-state initialization, depleting one of the statistical mixture states through continuous electron spin resonance (ESR) application during optical initialization. Nagy *et al.* have shown initialization fidelities of up to 97% [4]. However, the underlying mechanisms of both ESR-assisted depletion and nondepletion methods have not been thoroughly studied, limiting our understanding

*Corresponding author: sangyunlee@gist.ac.kr

of efficient initialization methods and theoretical limits. Recently, Morioka *et al.* [24] and Liu *et al.* [25] have conducted in-depth investigations into the transitions between the spin sublevels of the excited and ground states for $V1$ and $V2$ centers, focusing on the dynamics involved during optical pumping and subsequent relaxation phases. Building on the transition rates reported in these studies, our work aims to develop comprehensive rate models that not only incorporate optical resonance and ESR, but also account for their off-resonance effects. Through this model, we provide a detailed explanation of the initialization process and leverage this insight to optimize experimental parameters, thereby achieving high-fidelity deterministic spin-qubit initialization.

II. METHODS

A. Nine-state rate model

We investigate the photophysical dynamics of the $V1$ and $V2$ centers using a comprehensive rate model. This model considers four ground-state sublevels, four excited-state sublevels, and metastable states. The number of metastable states that should be considered for establishing comprehensive models is different for the $V1$ and $V2$ centers, as is discussed in the following. Radiative transitions and nonradiative ISC via the metastable state connect these levels as shown in Fig. 1(a). While both $V1$ and $V2$ centers are studied in this work, our focus is mainly on the $V1$ center, all of whose intrinsic transition rates have been revealed by thorough experiments at cryogenic temperatures [24]. We discuss both centers' photophysical dynamics but the quantitative model of only the $V1$ center is presented, while the discussions based on the incomplete set of the transition rates of the $V2$ center are provided in the Supplemental Material [26].

For both the $V1$ and $V2$ centers, there is a doublet metastable state between the excited and ground states that can be treated as a single level due to the fast transition between the doublet states, as discussed in previous studies [23,24] [see Fig. 1(a)]. However, for the $V2$ center, a recent study by Liu *et al*. based on new experimental data acquired at low optical pumping power has revealed that another higher lying metastable state must be considered [25]. Because this metastable state is shown to couple with another higher lying excited doublet state, which acts as a deshelving state, the ISC rates related to this state appear to be dependent on the optical pumping power and only a few values in the low optical pumping power range were obtained [25]. For this reason, a comprehensive rate model cannot be established for the $V2$ center in this work. However, we provide quantitative discussions using the known values for these rates under specific experimental conditions in the Supplemental Material [26]. Meanwhile, we focus on the $V1$ center as described in Fig. 1, which illustrates all transitions, such as optical pumping, radiative decay, nonradiative ISC, and ESR. The spin-conserving optical resonance transition between excited states and the ground state with $|m_S| = 1/2$ and $|m_S| = 3/2$ are referred to as $O1$ and $O2$ transitions, respectively, following the labeling in the recent research [25]. The ISC rates depend on $|m_S|$ in the excited state and the ground state [27], thus using only the $O1$ ($O2$) transition leads to an equal mixture of the two ground-state sublevels with $|m_S| = 3/2$ ($|m_S| = 1/2$) for both $V1$ and $V2$ centers [4,8,23], as can be seen in Fig. 1(b). This poses a challenge when utilizing the silicon vacancy in 4H-SiC and similar systems with odd-integer multiples of $S = 1/2$ for reliable quantum

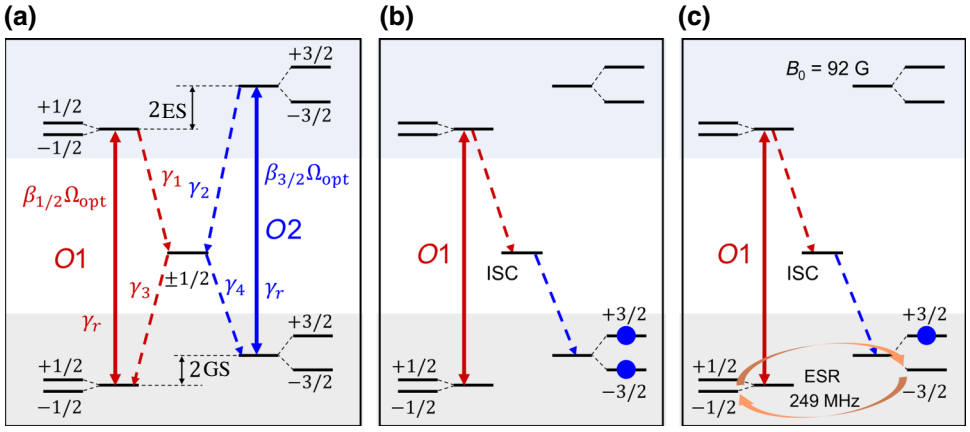

FIG. 1. (a) Spin sublevel structure of the silicon vacancy ($V1$ and $V2$ center) in 4H-SiC. Only the levels and rates that are common to both $V1$ and $V2$ centers are described. Another higher lying metastable state for the $V2$ center and related rates are not shown. Spin initialization mechanism resulting in (b) a mixed state using only the $O1$ transition and (c) a pure state using both the $O1$ transition and ESR. The thick solid red and blue lines represent optical resonant transitions $O1$ and $O2$, respectively. In (b),(c), only the dominant pathways for the initialization are depicted. Dashed lines represent ISC from and to the metastable states, and orange arrows represent ESR between $m_S = -1/2$ and $m_S = -3/2$ states. See text for detail.

TABLE I. The transition rates of the $V1$ center reported by Morioka *et al.* [24], as seen in Fig. 1(a).

	Decay time (ns)
$1/\gamma_r$	9.1
$1/\gamma_1$	11.3
$1/\gamma_2$	20.6
$1/\gamma_3$	540
$1/\gamma_4$	500

information technology. Recent studies have demonstrated selective single spin initialization for $V1$ and $V2$ centers, achieving initialization into a pure state [4,7]. This is accomplished through resonant optical pumping combined with ESR to redistribute the spin population. In the following sections, we delve into the detailed mechanisms and discuss strategies for achieving high-fidelity initialization efficiently.

B. Rate equation

We present a spin initialization mechanism utilizing resonant optical transitions and ESR, described by a rate model given in Eq. (1) for the $V1$ center.

$$\begin{aligned}
\dot{n}^{\mathrm{GS}}_{m_s}(t) &= -\beta_{m_s}\Omega_{\mathrm{opt}} n^{\mathrm{GS}}_{m_s}(t) + \gamma_r n^{\mathrm{ES}}_{m_s}(t) + \gamma_{i+2} n^{\mathrm{MS}}(t) \\
&\quad + W_{m_s-1,m_s}(n^{\mathrm{GS}}_{m_s-1}(t) - n^{\mathrm{GS}}_{m_s}(t)) \\
&\quad - W_{m_s,m_s+1}(n^{\mathrm{GS}}_{m_s}(t) - n^{\mathrm{GS}}_{m_s+1}(t)), \\
\dot{n}^{\mathrm{ES}}_{m_s}(t) &= \beta_{m_s}\Omega_{\mathrm{opt}} n^{\mathrm{GS}}_{m_s}(t) - (\gamma_r + \gamma_i) n^{\mathrm{ES}}_{m_s}(t), \\
\dot{n}(t) &= \Sigma^{3/2}_{m_s=-3/2}(\gamma_i n^{\mathrm{ES}}_{m_s}(t) - \gamma_{i+2} n^{\mathrm{MS}}(t)),
\end{aligned} \tag{1}$$

where $m_s = \pm 1/2, \pm 3/2$, $W_{-5/2,-3/2} = W_{3/2,5/2} = 0$, $i = |m_s| + 1/2$. The normalized population of each ground spin state with magnetic quantum number m_s is denoted as $n^{\mathrm{GS}}_{m_s}(t)$. Similarly, $n^{\mathrm{ES}}_{m_s}(t)$ and $n^{\mathrm{MS}}(t)$ represent the excited- and metastable-state populations, respectively. For convenience, we refer to $n^{\mathrm{GS}}_{m_s}(t)$, $n^{\mathrm{ES}}_{m_s}(t)$, and $n^{\mathrm{MS}}(t)$ as the initialization fidelity of the spin sublevels, as they represent the normalized population of each spin state achieved through the initialization process. The coefficients used in the model are defined as follows: Ω_{opt} represents the optical Rabi frequency, which is determined by the optical pumping rate; β_{m_s} represents the spin-conserving optical transition probability with m_s. The model also incorporates the radiative decay rate (γ_r), and the ISC rate (γ_i), and experimental parameters such as optical resonance frequency detuning $\delta\omega_{\mathrm{opt},m_s}$ and the laser linewidth $\Delta\nu_{\mathrm{opt}}$. See the Appendices A and B for details. The values used for the radiative decay and ISC rates are summarized in Table I. Additionally, the ESR transition rate between the sublevels with m_s and $m_s + 1$ in the ground state is denoted as W_{m_s,m_s+1}, which is explained in the following.

We define the Hamiltonian of the excited states and the ground states to calculate the transition rate resulting from ESR between the two sublevels of the ground state. The resulting ESR transition rate W_{m_s,m_s+1} is proportional to $\Omega_1^{m_s,m_s+1} = \sqrt{\left(\omega_1^{m_s,\,m_s+1}\right)^2 + \left(\Delta\omega_0^{m_s,m_s+1}\right)^2}$, which represents the spin-Rabi-nutation frequency. For the high-spin system, when the applied microwave strength is B_1, the spin-Rabi-nutation frequency varies with respect to $\omega_1 = 2\pi g\mu_B B_1/h$ depending on m_S and $m_S + 1$ of $S = 3/2$ through the relation $\omega_1^{m_s,\,m_s+1} = \omega_1\sqrt{S(S+1) - m_s(m_s+1)}$. Here, g is the Landé g factor of the electron spin and μ_B is the Bohr magneton. To account for the off-resonance effect and line broadening, the T_1 relaxation time and the detuning $\Delta\omega_0^{m_s,m_s+1} \equiv \omega_0^{m_s,m_s+1} - \omega_{\mathrm{MW}}$ are included. Here, $\omega_0^{m_s,m_s+1}$ represents the ESR frequency between the sublevels m_s and $m_s + 1$, and ω_{MW} is the applied microwave frequency. For further detail, see Appendix B.

III. RESULTS

A. Photoluminescence characteristics

To validate our rate model and compare it with previous experimental results, we simulate the photoluminescence (PL) intensity of the $V1$ center under resonant optical excitation. We aim to demonstrate the consistency of our model by presenting results that closely resemble the previously reported data [4,7,23,24].

We first present the PL intensity simulation with the $O1$ resonant pumping corresponding to the $|\pm 1/2\rangle_{\mathrm{GS}} \leftrightarrow |\pm 1/2\rangle_{\mathrm{ES}}$. An optical Rabi frequency $\Omega_{\mathrm{opt}}/2\pi = 2.6$ MHz and an external magnetic field parallel to the spin quantization axis (the c axis of 4H-SiC) $B_0 = 92$ G is used, and the initial ground state is assumed to be completely depolarized. Figure 2(a) represents the PL intensity changing in time during a 5-μs $O1$ optical resonance pumping without ESR. After the optical pumping at the $O1$ transition is switched on, it reaches its maximum value in 10 ns then it decays in approximately 3 μs. The $O1$ transition leads to the continuous pumping of the ground state $|\pm 1/2\rangle_{\mathrm{GS}}$ to the excited state $|\pm 1/2\rangle_{\mathrm{ES}}$, then decay to the ground state either directly via the spin-conserving $O1$ decay or through the metastable state via the ISC. The decay path through the ISC allows spin-flipping among the ground-state spin sublevels, thus the repetitive $O1$ resonant pumping will eventually lead to an accumulation of the $|\pm 3/2\rangle_{\mathrm{GS}}$ population with a higher probability by depleting the $|\pm 1/2\rangle_{\mathrm{GS}}$ population in both the $V1$ center [see Figs. 2(b) and 2(c)] and the $V2$ center (see Supplemental Material [26]). This process is depicted in Fig. 1(b). The time evolution of the ground-state spin sublevel populations of the $V1$ center, initially depolarized but becoming polarized into the $|\pm 3/2\rangle_{\mathrm{GS}}$ sublevels due to the $O1$ excitation, is shown

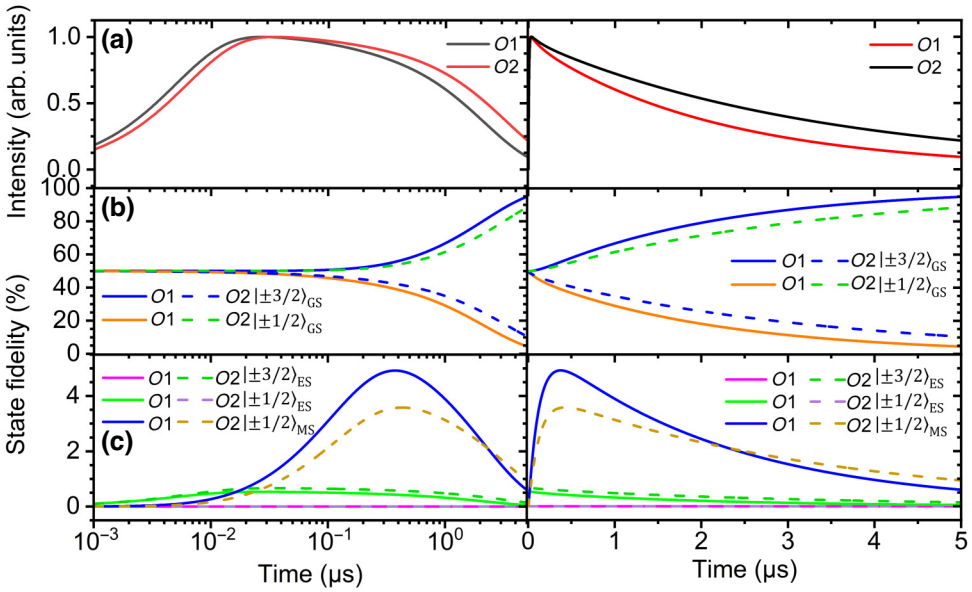

FIG. 2. With the $O1$ and $O2$ optical resonances, (a) the PL intensity, and the fidelity of spin sublevels of (b) ground state and (c) excited state. Left column is in log scale, and right column is in linear scale.

in Figs. 2(b) and 2(c). Although the ISC rates are spin-dependent, because the optical initialization using the resonance optical transition leads to depletion of the pumped states as explained previously, optical pumping at any resonance frequencies results in the equal mixture of two unpumped spin sublevels in the ground state. Therefore, the $O2$ resonant pumping will induce a similar time evolution of the sublevel populations as seen in Figs. 2(b) and 2(c). These results demonstrate that our established model successfully captures the statistical mixture of the two sublevels of the silicon vacancies in 4H-SiC when only optical pumping is employed, aligning with the previous works. [4,7,23,24].

Our rate model also provides a comprehensive explanation for the photoluminescence excitation (PLE) spectra, in agreement with previous experimental studies [4,7,23]. We observe that the intensity differences between the two characteristic peaks originating from the $O1$ and $O2$ transitions are primarily influenced by the ISC. Additionally, the degree of polarization in the ground state prior to the optical pumping has a significant impact on the peak intensity difference. It is important to note that, in typical experimental conditions, achieving complete depolarization is challenging, which may lead to misleading observations of the peak intensity difference. Further details can be found in the Supplemental Material [26].

B. Selective initialization

We investigate the combined method of optical pumping and ESR for selective initialization of specific spin sublevels in the ground state. While the $O1$ pumping leads to the accumulation of the $|\pm 3/2\rangle_{\mathrm{GS}}$ [Fig. 2(a)], the simultaneous ESR corresponding to $|-3/2\rangle_{\mathrm{GS}} \leftrightarrow |-1/2\rangle_{\mathrm{GS}}$ transfers the population from $|-3/2\rangle_{\mathrm{GS}}$ to $|-1/2\rangle_{\mathrm{GS}}$. The population transferred to $|-1/2\rangle_{\mathrm{GS}}$ will be pumped again by the $O1$ transition. Repeating this process depletes the $|-3/2\rangle_{\mathrm{GS}}$ population as well, resulting in the accumulation of the $|+3/2\rangle_{\mathrm{GS}}$ population. Consequently, ESR of $|\pm 3/2\rangle_{\mathrm{GS}} \leftrightarrow |\pm 1/2\rangle_{\mathrm{GS}}$ combined with the $O1$ optical pumping enables the $|\mp 3/2\rangle_{\mathrm{GS}}$ state initialization. Alternatively, when using the $O2$ resonant transition, which yields a higher population of $|\pm 1/2\rangle_{\mathrm{GS}}$ [Fig. 2(b)], the simultaneous ESR of $|\pm 1/2\rangle_{\mathrm{GS}} \leftrightarrow |\pm 3/2\rangle_{\mathrm{GS}}$ results in the $|\mp 1/2\rangle_{\mathrm{GS}}$ state initialization. To quantify the effectiveness of each process, we calculate the initialization fidelity from the populations of the spin sublevels after a 1-ms initialization sequence, followed by a waiting time of 0.5 μs to allow for the decay of all the excited-state populations back to the ground state. Longer initialization time leads to the higher fidelities. Applying an initialization sequence longer than 1 ms is indeed possible, since the silicon vacancy in SiC is known to have a T_1 relaxation time of over 1 s [9]. However, we restrict the initialization sequence time to 1 ms, which is a rough maximum value in typical experimental conditions.

Figure 3 shows the state fidelity during a 1-ms excitation laser centered at the $O1$ transition combined with the ESR of $|-3/2\rangle_{\mathrm{GS}} \leftrightarrow |-1/2\rangle_{\mathrm{GS}}$. The optimal parameters used in the simulations that lead to the best fidelity are an optical Rabi frequency ($\Omega_{\mathrm{opt}}/2\pi$) of 2.6 MHz and a spin-Rabi frequency ($\omega_1/2\pi$) of 0.05 MHz. The optimal conditions are discussed in the following. The state fidelities of the ground sublevels, and the excited and metastable states are

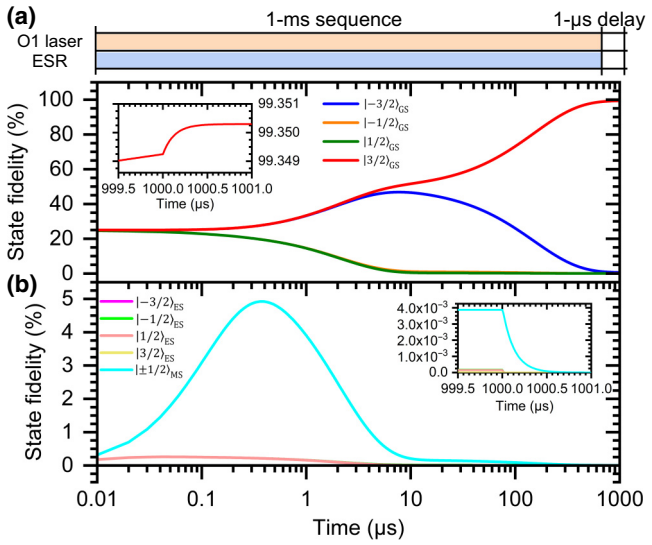

FIG. 3. State fidelities of (a) the ground-state sublevels, (b) excited and metastable states during the 1-ms excitation laser of the $O1$ transition and $|-3/2\rangle_{GS} \leftrightarrow |-1/2\rangle_{GS}$ ESR, followed by 1-μs delay. Inset in (a) shows the $|3/2\rangle_{GS}$ fidelity after turning off the laser. In (b), $|-1/2\rangle_{GS}$ and $|+1/2\rangle_{GS}$ fidelities almost overlap and go to zero after 10 μs, and $|3/2\rangle_{ES}$ and $|-3/2\rangle_{ES}$ fidelities are almost zero. Inset in (b) shows the excited-state fidelities after turning off the laser. See text for detail.

shown in Figs. 3(a) and 3(b), respectively. The fidelities of $|\pm 1/2\rangle_{ES}$ and $|\pm 1/2\rangle_{MS}$ initially increase until 0.1 μs and then start exponentially decreasing at around 1 μs due to the applied approximate 1-MHz optical Rabi transition [Fig. 3(b)]. At this timescale, all other excited-state populations remain zero due to the selective $O1$ transition. The depletion of $|\pm 1/2\rangle_{ES}$ and $|\pm 1/2\rangle_{MS}$ originates from the noncyclic transition behavior of the $O1$ transition at long timescales due to the slow ISC. While the fidelities of the excited state show a decline within 10 μs, those of $|\pm 3/2\rangle_{GS}$ start to increase. The state fidelity of $|-3/2\rangle_{GS}$ starts decreasing at around 10 μs when the ESR of the approximately 0.05-MHz spin-Rabi frequency transfers the population from $|-3/2\rangle_{GS}$ to $|-1/2\rangle_{GS}$. The transferred population of $|-3/2\rangle_{GS}$ eventually adds to $|+3/2\rangle_{GS}$ via the path from $|-1/2\rangle_{GS}$ to $|-1/2\rangle_{ES}$ ($O1$ transition) and from $|-1/2\rangle_{ES}$ to $|+3/2\rangle_{GS}$ (ISC). Even if the population of $|-3/2\rangle_{GS}$ follows alternative paths, e.g., $|-1/2\rangle_{GS} \rightarrow |-1/2\rangle_{ES} \rightarrow |\pm 1/2\rangle_{MS} \rightarrow |+1/2\rangle_{GS}$, it eventually follows the desired path after several repetitions when the initialization sequence is sufficiently long. This selective initialization mechanism is depicted in Fig. 1(c). After turning off the initialization sequence, the remaining excited-state populations decay to the ground state, resulting in a slight increase in the state fidelity of $|-3/2\rangle_{GS}$, as in the inset of Fig. 3(a).

C. The optimal conditions

We have found the selective initialization mechanism, and figured out which ground-state sublevel is initialized by the applied experimental parameters. Through extensive testing of various parameter sets, we have identified the key experimental factors that significantly influence the initialization fidelity: optical resonance frequency detuning $\delta\omega_{\mathrm{opt},m_s}$, optical Rabi frequency Ω_{opt}, ESR frequency detuning $\Delta\omega_0^{m_s,m_s+1}$, spin-Rabi frequency ω_1, and the initialization sequence length. It turns out that setting the optical resonance frequency detuning and ESR frequency detuning to zero, i.e., $\delta\omega_{\mathrm{opt},m_s} = 0$ and $\Delta\omega_0^{m_s,m_s+1} = 0$, yields the highest fidelities (see Supplemental Material [26]).

To determine the conditions that maximize the initialization fidelity within a 1-ms sequence, we vary the optical Rabi frequency of the $O1$ transition and the spin-Rabi frequency of the ESR. As a result, we achieve a maximum state fidelity of 99.35% in $|\pm 3/2\rangle_{GS}$ when the optical Rabi frequency is set to 2.6 MHz and the spin-Rabi frequency is set to 0.05 MHz, as shown in Fig. 4. Weak optical pumping leads to slow initialization, while slow ESR results in a low probability of depleting one of the optically polarized sublevels. Hence, fast optical pumping and ESR lead to the faster saturation of the initialization fidelity, as explained in the Supplemental Material [26]. However, there exists a trade-off. If either or both frequencies exceed the optimal values, the target sublevel $|\pm 3/2\rangle_{GS}$ becomes susceptible to optical pumping then may decay to other sublevels, potentially being depleted by the ESR. Thus, a stronger off-resonance effect that originates from large Ω_{opt} and ω_1 increases the probability of mixing with other spin sublevels, thereby reducing the fidelity. It is important to

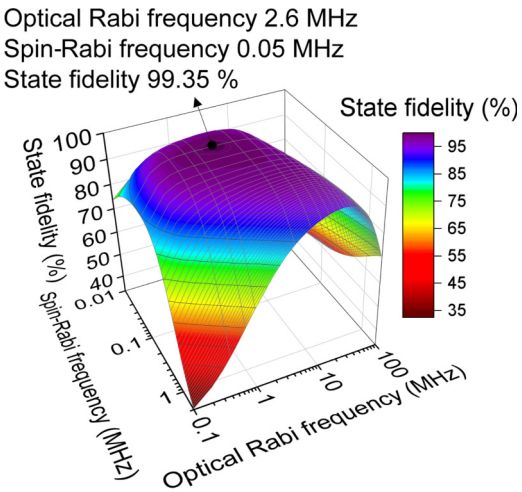

FIG. 4. Initialized state fidelity of $|\pm 3/2\rangle_{GS}$ as a function of optical Rabi frequency and spin-Rabi frequency under a 1-ms sequence.

TABLE II. The initialized state with the best fidelity obtained by the optimum conditions by the 1-ms initialization sequence.

ESR	$O1$ transition	$O2$ transition
$\|3/2\rangle_{GS} \leftrightarrow \|1/2\rangle_{GS}$	$\|-3/2\rangle_{GS}$ (99.35%)	$\|-1/2\rangle_{GS}$ (97.10%)
$\|-3/2\rangle_{GS} \leftrightarrow \|-1/2\rangle_{GS}$	$\|3/2\rangle_{GS}$ (99.35%)	$\|1/2\rangle_{GS}$ (97.11%)

note that if the off-resonance effect is weakened, a longer sequence can be utilized to achieve higher fidelity.

Table II summarizes the optimal conditions and outcomes for selectively initializing the ground-state spin sublevels using different combinations of optical transitions and ESR frequencies. As explained previously, the $O1$ ($O2$) transition must be employed to selectively initialize $|+3/2\rangle_{GS}$ or $|-3/2\rangle_{GS}$ ($|+1/2\rangle_{GS}$ or $|-1/2\rangle_{GS}$). Table II also presents the highest fidelities achieved for the initialized states through parameter optimization. The initialization process utilizing the $O1$ transition with ESR yields a higher fidelity by approximately 2% compared with the process involving the $O2$ transition. We attribute this higher fidelity (99.35%) to the twofold faster ISC decay rate from the $|\pm 1/2\rangle_{ES}$ sublevels (γ_1) compared with the $|\pm 3/2\rangle_{ES}$ sublevels (γ_2). Consequently, as the sequence time increases, both fidelities converge to a common value (see the Supplemental Material [26]).

IV. CONCLUSIONS

We investigate, by establishing a comprehensive rate model, the mechanism of the selective spin initialization technique of the silicon vacancy in silicon carbide that utilizes both laser excitation and ESR as previously demonstrated in experimental studies [4,7]. By depleting undesired spin sublevels through ESR in the ground states, we find that a selective initialization with a fidelity of up to 99.35% using an optimized 1-ms initialization sequence can be achieved, which is better than the previously reported best value of 97% [4]. The $O1$ optical transition exhibits higher fidelity compared with the $O2$ transition, primarily due to differences in ISC rates. Notably, while higher power levels of the resonant laser and ESR lead to faster initialization, they also introduce off-resonance effects that reduce the fidelity. The high fidelity attained through this mechanism highlights its potential for initializing the silicon-vacancy spin qubit in a pure state. The selectively initialized spin-qubit state holds promise for various quantum information applications, including quantum state tomography of the $S = 3/2$ qubit, high-fidelity universal quantum processors based on the multinuclear spin system bound to silicon-vacancy electronic spins [28], and entanglement of remote quantum repeaters. By clarifying the selective initialization mechanism and providing understanding about the behavior of fidelities under various key parameters, our study not only provides an accurate description of the selective spin initialization mechanism in the silicon vacancy of silicon carbide but also underscores the potential of this system for spin-based quantum information technologies.

ACKNOWLEDGMENTS

We thank Naoya Morioka for fruitful discussions. This research was supported by the National Research Foundation of Korea (NRF) funded by the Korean government [Ministry of Science and ICT (MSIT)] (Grants No. 2021M3H3A1037899 and No. 2021R1A2C2006904), and the Institute of Information & communication Technology Planning & Evaluation (IITP) grant funded by the Korean government (MSIT) (Grant No. 2022-0-00198).

APPENDIX A: OPTICAL TRANSITIONS

The optical Rabi frequency Ω_{opt} is a function proportional to the square root of the laser power of the resonant laser. The laser used for the $O1$ or $O2$ transition cannot be perfectly selective since the linewidth is finite. The laser linewidth is assumed to be $\Delta\nu_{opt} = 1$ MHz because the previous experimental research [4,7,23,29] used a pump laser to measure the ZPL linewidth and found it to be a minimum of 29 MHz. The detuning corresponding to the difference between the laser frequency and each resonant frequency is $\delta\omega_{opt,m_s} = \omega_{opt} - \omega_{opt,m_s}$. ω_{opt} is the laser frequency and $\omega_{opt,\,m_s}$ is the frequency difference between the excited and ground state sublevels with the common spin quantum number m_S. Since the $O1$ and $O2$ transitions are spin-conserving, the detuning is presented as $\delta\omega_{opt,m_s}$ in the main text. Regarding the off-resonant effect, when a laser with a specific frequency ω_{opt} and linewidth $\Delta\nu_{opt}$ are given, the optical transition probability β_{m_s} between sublevel i and sublevel j with the same m_s is described as in Eq. (A1).

$$\beta_{m_s} = \Omega_{opt}\frac{\Omega_{opt} + \Delta\nu_{opt}/2}{(\Omega_{opt} + \Delta\nu_{opt}/2)^2 + \delta\omega_{opt,m_s}{}^2}. \tag{A1}$$

APPENDIX B: SPIN SUBLEVELS

We introduce the Hamiltonian of the excited states, and the ground states as follows:

$$H_{GS} = g\mu_B S\cdot B_0 + D_{GS}\left[S_z^2 - \frac{S(S+1)}{3}\right] + E_{GS}[S_x^2 - S_y^2], \tag{B1}$$

$$H_{ES} = g\mu_B S\cdot B_0 + D_{ES}\left[S_z^2 - \frac{S(S+1)}{3}\right] + E_{ES}[S_x^2 - S_y^2] + E_0. \tag{B2}$$

Here, g is Landé g factor, μ_B is Bohr magneton. The Hamiltonian includes the Zeeman effect term (first term)

due to the static external magnetic field B_0 with c-axis direction parallel to the $V1$ and $V2$ center spin quantization axis [30]. The zero-field splitting (ZFS) terms due to the spin-spin dipole interaction (second and third terms) are also included [31,32]. The last term in the excited-state Hamiltonian, E_0, represents the energy difference between the ground state and excited state without the electronic spins. The ZFS parameters of the ground state and the excited state are known as $2D_{GS} = 4.5$ MHz and $2D_{ES} = 1$ GHz for the $V1$ center and $2D_{GS} = 70$ MHz and $2D_{ES} = 1$ GHz for the $V2$ center, and $E_{GS} = E_{ES} = 0$ due to the uniaxial symmetry [4,7,8,23]. From the ground-state Hamiltonian, we can calculate the ESR transition rate

$$W_{m_s,\, m_s+1} = \Omega_1^{m_s,\, m_s+1} \frac{\omega_1^{(m_s,\, m_s+1)}\left(\omega_1^{(m_s,\, m_s+1)} + (2\pi/T_1)\right)}{\Delta\omega_0^{(m_s,\, m_s+1)^2} + \left(\omega_1^{(m_s,\, m_s+1)} + (2\pi/T_1)\right)^2}, \tag{B3}$$

where $\omega_1^{(m_s,\, m_s+1)}$ is the spin-Rabi-nutation frequency given as $\omega_1^{(m_s,\, m_s+1)} = \omega_1\sqrt{S(S+1) - m_{S,m_s} m_{S,m_s+1}}$, with $\omega_1 = g\mu_B B_1/2\pi h$ and $S = 3/2$. For example, $\omega_1^{(1/2,3/2)} = \sqrt{3}\omega_1$ for $m_{S,m_s} = 1/2$ and $m_{S,m_s+1} = 3/2$, and $\omega_1^{(-1/2,1/2)} = 2\omega_1$ for $m_{S,m_s} = -1/2$ and $m_{S,m_s+1} = 1/2$. This nutation frequency correction is successfully used to confirm that the $V1$ and $V2$ centers have $S = 3/2$ [4,33]. The spin-resonance transition frequency between two ground-state sublevels m_s and $m_s + 1$, i.e., $\omega_0^{(m_s,\, m_s+1)}$, is calculated from the spin Hamiltonian in Eqs. (B1) and (B2) and the applied microwave frequency to induce the magnetic resonance effect is ω_{MW}. The detuning of the microwave frequency with respect to $\omega_0^{(m_s,\, m_s+1)}$ is $\Delta\omega_0^{(m_s,\, m_s+1)} \equiv \omega_0^{(m_s,\, m_s+1)} - \omega_{MW}$ and the spin-Rabi frequency considering the detuning is given by $\Omega_1^{m_s,\, m_s+1} = \sqrt{\omega_1^{(m_s,\, m_s+1)^2} + \Delta\omega_0^{(m_s,\, m_s+1)^2}}$. Applying all, we calculate the population of each sublevel established by the initialization sequences to estimate the spin initialization fidelities.

[1] I. Aharonovich, D. Englund, and M. Toth, Solid-state single-photon emitters, Nat. Photonics **10**, 631 (2016).

[2] D. D. Awschalom, R. Hanson, J. Wrachtrup, and B. B. Zhou, Quantum technologies with optically interfaced solid-state spins, Nat. Photonics **12**, 516 (2018).

[3] M. Atatüre, D. Englund, N. Vamivakas, S.-Y. Lee, and J. Wrachtrup, Material platforms for spin-based photonic quantum technologies, Nat. Rev. Mater. **3**, 38 (2018).

[4] R. Nagy, M. Niethammer, M. Widmann, Y.-C. Chen, P. Udvarhelyi, C. Bonato, J. U. Hassan, R. Karhu, I. G. Ivanov, N. T. Son, *et al.*, High-fidelity spin and optical control of single silicon-vacancy centres in silicon carbide, Nat. Commun. **10**, 1954 (2019).

[5] M. Widmann, M. Niethammer, D. Y. Fedyanin, I. A. Khramtsov, T. Rendler, I. D. Booker, J. Ul Hassan, N. Morioka, Y.-C. Chen, I. G. Ivanov, *et al.*, Electrical charge state manipulation of single silicon vacancies in a silicon carbide quantum optoelectronic device, Nano Lett. **19**, 7173 (2019).

[6] P. Udvarhelyi, R. Nagy, F. Kaiser, S.-Y. Lee, J. Wrachtrup, and A. Gali, Spectrally stable defect qubits with no inversion symmetry for robust spin-to-photon interface, Phys. Rev. Appl. **11**, 044022 (2019).

[7] C. Babin, R. Stöhr, N. Morioka, T. Linkewitz, T. Steidl, R. Wörnle, D. Liu, E. Hesselmeier, V. Vorobyov, A. Denisenko, *et al.*, Fabrication and nanophotonic waveguide integration of silicon carbide colour centres with preserved spin-optical coherence, Nat. Mater. **21**, 67 (2022).

[8] M. Widmann, S.-Y. Lee, T. Rendler, N. T. Son, H. Fedder, S. Paik, L.-P. Yang, N. Zhao, S. Yang, I. Booker, *et al.*, Coherent control of single spins in silicon carbide at room temperature, Nat. Mater. **14**, 164 (2015).

[9] D. Simin, H. Kraus, A. Sperlich, T. Ohshima, G. V. Astakhov, and V. Dyakonov, Locking of electron spin coherence above 20 ms in natural silicon carbide, Phys. Rev. B **95**, 161201 (2017).

[10] N. T. Son, C. P. Anderson, A. Bourassa, K. C. Miao, C. Babin, M. Widmann, M. Niethammer, J. Ul Hassan, N. Morioka, I. G. Ivanov, *et al.*, Developing silicon carbide for quantum spintronics, Appl. Phys. Lett. **116**, 190501 (2020).

[11] M. Niethammer, M. Widmann, T. Rendler, N. Morioka, Y.-C. Chen, R. Stöhr, J. U. Hassan, S. Onoda, T. Ohshima, S.-Y. Lee, *et al.*, Coherent electrical readout of defect spins in silicon carbide by photo-ionization at ambient conditions, Nat. Commun. **10**, 5569 (2019).

[12] Y. Chiba, Y. Yamazaki, T. Makino, S. I. Sato, N. Yamada, T. Satoh, K. Kojima, S. Y. Lee, Y. Hijikata, and T. Ohshima, Creation of color centers in SiC PN diodes using proton beam writing, Mater. Sci. Forum **963**, 709 (2019).

[13] M. Widmann, M. Niethammer, T. Makino, T. Rendler, S. Lasse, T. Ohshima, J. Ul Hassan, N. Tien Son, S.-Y. Lee, and J. Wrachtrup, Bright single photon sources in lateral silicon carbide light emitting diodes, Appl. Phys. Lett. **112**, 231103 (2018).

[14] S.-i. Sato, T. Honda, T. Makino, Y. Hijikata, S.-Y. Lee, and T. Ohshima, Room temperature electrical control of single photon sources at 4H-SiC surface, ACS Photonics **5**, 3159 (2018).

[15] B.-S. Song, T. Asano, S. Jeon, H. Kim, C. Chen, D. D. Kang, and S. Noda, Ultrahigh-Q photonic crystal nanocavities based on 4H silicon carbide, Optica **6**, 991 (2019).

[16] D. M. Lukin, C. Dory, M. A. Guidry, K. Y. Yang, S. D. Mishra, R. Trivedi, M. Radulaski, S. Sun, D. Vercruysse, G. H. Ahn, and J. Vučković, 4H-silicon-carbide-on-insulator for integrated quantum and nonlinear photonics, Nat. Photonics **14**, 330 (2020).

[17] D. M. Lukin, M. A. Guidry, and J. Vučković, Integrated quantum photonics with silicon carbide: Challenges and prospects, PRX Quantum **1**, 020102 (2020).

[18] S. Castelletto and A. Boretti, Silicon carbide color centers for quantum applications, J. Phys.: Photonics **2**, 022001 (2020).

[19] T. Nishikawa, N. Morioka, H. Abe, H. Morishita, T. Ohshima, and N. Mizuochi, Electrical detection of nuclear

spins via silicon vacancies in silicon carbide at room temperature, Appl. Phys. Lett. **121**, 184005 (2022).

[20] E. Sörman, N. T. Son, W. M. Chen, O. Kordina, C. Hallin, and E. Janzén, Silicon vacancy related defect in 4H and 6H SiC, Phys. Rev. B **61**, 2613 (2000).

[21] S. Barnett, *Quantum Information* (Oxford University Press, New York, 2009), Vol. 16.

[22] I. Aharonovich, S. Castelletto, D. A. Simpson, A. D. Greentree, and S. Prawer, Photophysics of chromium-related diamond single-photon emitters, Phys. Rev. A **81**, 043813 (2010).

[23] H. B. Banks, ÖO Soykal, R. L. Myers-Ward, D. K. Gaskill, T. L. Reinecke, and S. G. Carter, Resonant optical spin initialization and readout of single silicon vacancies in 4H-SiC, Phys. Rev. Appl. **11**, 024013 (2019).

[24] N. Morioka, D. Liu, ÖO Soykal, I. Gediz, C. Babin, R. Stöhr, T. Ohshima, N. T. Son, J. Ul-Hassan, F. Kaiser, and J. Wrachtrup, Spin-optical dynamics and quantum efficiency of a single V1 center in silicon carbide, Phys. Rev. Appl. **17**, 054005 (2022).

[25] D. Liu, F. Kaiser, V. Bushmakin, E. Hesselmeier, T. Steidl, T. Ohshima, N. T. Son, J. Ul-Hassan, ÖO Soykal, and J. Wrachtrup, The silicon vacancy centers in SiC: determination of intrinsic spin dynamics for integrated quantum photonics, arXiv preprint arXiv:2307.13648 (2023).

[26] See Supplemental Material at http://link.aps.org/supplemental/10.1103/PhysRevApplied.21.054005 for additional results and the $V1$ center rate model.

[27] ÖO Soykal, P. Dev, and S. E. Economou, Silicon vacancy center in 4H-SiC: Electronic structure and spin-photon interfaces, Phys. Rev. B **93**, 081207 (2016).

[28] S. K. Parthasarathy, B. Kallinger, F. Kaiser, P. Berwian, D. B. R. Dasari, J. Friedrich, and R. Nagy, Scalable quantum memory nodes using nuclear spins in silicon carbide, Phys. Rev. Appl. **19**, 034026 (2023).

[29] N. Morioka, C. Babin, R. Nagy, I. Gediz, E. Hesselmeier, D. Liu, M. Joliffe, M. Niethammer, D. Dasari, V. Vorobyov, *et al.*, Spin-controlled generation of indistinguishable and distinguishable photons from silicon vacancy centres in silicon carbide, Nat. Commun. **11**, 2516 (2020).

[30] E. Janzén, A. Gali, P. Carlsson, A. Gällström, B. Magnusson, and N. T. Son, The silicon vacancy in SiC, Phys. B **404**, 4354 (2009).

[31] N. M. Atherton, *Principles of Electron Spin Resonance* (Ellis Horwood, Chichester, 1993). Ellis Horwood PTR Prentice Hall physical chemistry series.

[32] S.-Y. Lee, M. Niethammer, and J. Wrachtrup, Vector magnetometry based on $S = 3/2$ electronic spins, Phys. Rev. B **92**, 115201 (2015).

[33] N. Mizuochi, S. Yamasaki, H. Takizawa, N. Morishita, T. Ohshima, H. Itoh, and J. Isoya, Continuous-wave and pulsed EPR study of the negatively charged silicon vacancy with $S = 3/2$ and $C3v$ symmetry in n-type 4H-SiC, Phys. Rev. B **66**, 235202 (2002).